Plasma Phys. Control. Fusion 67 (2025) 085025 (12pp)

https://doi.org/10.1088/1361-6587/adf91b

Zonal flow suppression of turbulent transport in the optimized stellarators W7-X and QSTK

Abhishek Tiwari^{1,*}, Joydeep Das¹, Jaya Kumar Alageshan¹, Gareth Roberg-Clark², Gabriel Plunk², Pavlos Xanthopoulos², Sarveshwar Sharma^{3,4}, Zhihong Lin⁵ and Animesh Kuley^{1,*}

E-mail: abhishektiwa@iisc.ac.in and akuley@iisc.ac.in

Received 22 January 2025, revised 9 July 2025 Accepted for publication 7 August 2025 Published 20 August 2025



Abstract

We present a comparative study of transport in two optimized stellarator configurations: Wendelstein 7-X (W7-X) and a recent design called quasi-symmetric turbulence konzept (QSTK). Using global gyrokinetic toroidal code, we explore the role of zonal flows (ZFs) in suppressing electrostatic ion temperature gradient (ITG) driven turbulence in both configurations. The simulations reveal that ZFs significantly reduce ion heat transport in both W7-X and QSTK, with a lower value of heat flux on the latter configuration, as suggested by the apparently higher linear threshold ('critical') gradients for ITG modes. The study also highlights that both stellarators exhibit similar mode structures. The results support the notion that linear stability measures, in combination with nonlinear stabilization by ZFs, can play an important role in the suppression of nonlinear heat fluxes.

Keywords: simulations, gyrokinetic, microturbulence, stellarator, zonal flow

1. Introduction

Recent advancements in stellarator [1, 2] design and technology have significantly improved their plasma confinement capabilities, rendering them an increasingly promising approach in fusion research alongside the well-established tokamak designs. The stellarator has advantages over the tokamak, for instance, the toroidal current, steady state operation, and lower magnetohydrodynamic (MHD) activity. However, these advantages come at the cost of breaking toroidal symmetry, which can lead to an increase in collisional transport,

coupling of macro- and micro-instabilities, and stronger damping of zonal flows [3, 4]. Design and optimization [5] of stellarators have led to better plasma confinement in cases like Wendelstein 7-X (W7-X) [6], which have achieved a performance closer to tokamaks. It has been confirmed that neoclassical transport in W7-X is reduced with respect to nonoptimized stellarators [5, 7]. However, turbulence has played a dominant role in limiting plasma performance in W7-X for specific heating scenarios [8].

A primary obstacle in plasma confinement is the excitation of micro-instabilities such as the ion temperature gradient (ITG) and the trapped electron mode (TEM). Turbulence associated with these drift wave instabilities can degrade plasma confinement by transporting energy and particles. In modern stellarator experiments such as W7-X, advanced diagnostic

¹ Department of Physics, Indian Institute of Science, Bangalore 560012, India

² Max-Planck-Institut für Plasmaphysik, Greifswald 17491, Germany

³ Institute for Plasma Research, Bhat, Gandhinagar 382428, India

⁴ Homi Bhabha National Institute, Anushaktinagar, Mumbai, Maharashtra 400094, India

⁵ Department of Physics and Astronomy, University of California, Irvine, CA 92697, United States of America

^{*} Authors to whom any correspondence should be addressed.

techniques like phase contrast imaging are employed to measure and characterize ITG and TEM behavior [9]. It has been found that the stability of the ITG mode depends upon the gradient ratio $\eta_i = L_{n_i}/L_{T_i}$, where $1/L_X = -(1/X)(dX/dr)$ is the gradient length scale. The critical gradient (CG) is the threshold gradient for the onset of the ITG mode. One way to combat losses from ITG is to increase the size and heating power of the stellarator [10]. Another way is to address ITG itself by changing the plasma profiles [11]. Also, radio frequency waves can be used to stabilize these micro-instabilities in fusion plasmas [12, 13].

In addition to these strategies, shaping the magnetic field can further reduce losses due to micro-turbulence in the plasma core. Certain implementations of this strategy target the CG of the mode [10], (CG-approach), producing the HSK stellarator, which exhibits the most significant CG at half radius of all known stellarators. It has also been shown in [10] that this strategy can target the CG of the toroidal branch of the ITG mode without compromising MHD stability. Such optimization produces a quasi-helical symmetric configuration quasi-symmetric turbulence konzept (QSTK) with strongly reduced ITG turbulence and acceptable levels of neoclassical losses, and MHD stability, leading to improved ion confinement.

The QSTK configuration, as visualized alongside W7-X in figure 1, has $N_{\rm fp}=6$, an aspect ratio of 7.5, neoclassical transport coefficient $\epsilon_{\rm eff}<1\%$ up to half radius, large rotational transform >1.6 and $\simeq 5\%$ alpha particle neoclassical losses for particles initialized at half radius. QSTK also features good MHD stability, small bootstrap current, and it admits coils of moderate complexity. In addition, flux-tube based gyrokinetic simulations suggest that the heat flux is significantly reduced compared to W7-X [10].

Several gyrokinetic simulations of micro-turbulence in stellarators have been done previously. For example, the global code EUTERPE [14, 15] was used to study the effects of radial electric field on linear ITG instability in W7-X and LHD [16]. The effect of density gradient and micro-instabilities on turbulent heat transport in stellarators was performed with flux-tube code stella[17]. The electromagnetic gyrokinetic Vlasov flux-tube code GKV was used to study the impact of isotope ion mass on TEM driven turbulence and zonal flow (ZF) in LHD stellarators [18]. The GENE flux-tube simulation has been used to study the effect of ZF dynamics and turbulent transport in stellarator geometry [19]. The codes GENE-3D, KNOSOS, and TANGO were used to compute the plasma profiles due to the combined effect of neoclassical transport, turbulent transport, and external particles in W7-X, QSTK and HSK stellarators [20, 21]. The GT5D code performed full-f global simulations in LHD and the collisionless ZF damping [22]. Global XGC-S [23] and GENE-3D [24] were used to carry out micro-turbulence simulations using adiabatic electrons in W7-X and LHD. The global gyrokinetic toroidal code (GTC) was used to perform the nonlinear global gyrokinetic simulations of micro-turbulence in LHD and W7-X, including the kinetic effect of electrons in stellarators [3, 25, 26]. In addition to these efforts, global fluid simulation of plasma turbulence in stellarators has been carried out using the GBS [27] and BSTING [28, 29] codes.

In previous works [3, 25, 26], the global GTC has been used to perform nonlinear global gyrokinetic simulations of micro-turbulence in LHD and W7-X, including the benchmark of ITG simulations with EUTERPE [30], the suppression of ITG by neoclassical ambipolar electric field and its effects on microturbulence in W7-X stellarator [31], the isotope effects [32], the geometry effect on ZF [33], and the kinetic effect of electrons in stellarators. In this paper, we compare the effect of ZF on the turbulent transport driven by ITG turbulence with adiabatic electrons for the stellarators W7-X and QSTK. Recently, Carralero et al, have shown agreement between the experimental observations and the gyrokinetic simulation of low-frequency ZF using local (Stella) and global (EUTERPE) codes [34]. Also, it is important to mention that these simulations are very long and focused explicitly on resolving very low-frequency (sub-kHz) oscillation to compare specifically with the experimental measurements. The paper is organized as follows: First, in section 2, we briefly present the physics model and the numerical code employed. Then, in section 3, we study the linear simulation of ITG in both stellarators. In section 4, we perform the nonlinear simulations and evaluate the effect of ZF on the ITG turbulence. We conclude with some discussion in section 5.

2. Simulation model

In this paper, we use the global nonlinear code GTC [35] to perform collisionless gyrokinetic simulations of microturbulence. GTC has been extensively applied to simulate neoclassical and turbulent transport [26, 36–39], Alfvén waves [40, 41], energetic particles [42, 43], and radio frequency waves [44–46] in toroidally confined plasmas.

GTC interfaces with VMEC [47], an ideal MHD code, to obtain the non-axisymmetric equilibrium of QSTK and standard W7-X configuration, considering closed magnetic surfaces. This equilibrium data contains information on poloidal current, toroidal current, and magnetic field described as Fourier series in poloidal and toroidal direction, given by,

$$\mathcal{F}(\psi, \theta, \zeta) = \sum_{n} \left[\mathcal{F}_{c}(\psi, \theta, n) \cos(n\zeta) + \mathcal{F}_{s}(\psi, \theta, n) \sin(n\zeta) \right]$$

where (ψ, θ, ζ) are the poloidal flux, poloidal angle and toroidal angle, respectively. Here, n is the toroidal harmonic number and \mathcal{F}_c and \mathcal{F}_s are the Fourier coefficients specified on rectangular equilibrium mesh on the $\zeta = const.$ poloidal plane. GTC uses a global field-aligned mesh in real-space coordinates, which is used to represent all turbulence quantities. This provides computational efficiency without imposing any geometrical approximations and only needs a small number of grid points in the parallel directions to resolve the drift-wave

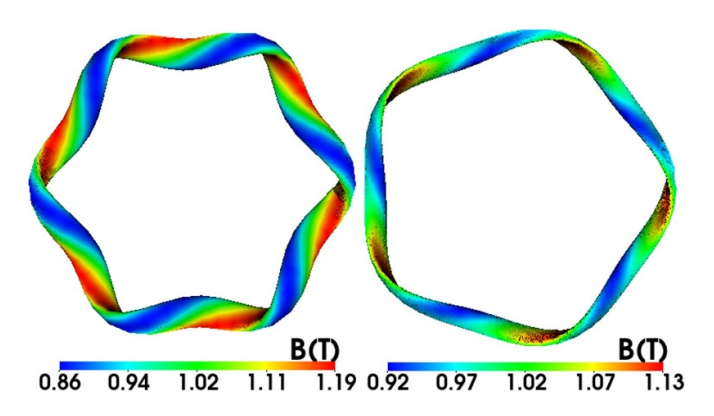


Figure 1. The magnetic field of the two stellarators: (left) QSTK; (right) W7-X on the flux surface with $\psi/\psi_{\rm w}=0.57$; the colors represent the corresponding strength of the magnetic fields.

eigenmode structure due to the anisotropic nature of microturbulence. Due to the toroidal asymmetry in stellarators, more toroidal grid points are required than tokamak for generating 3D equilibrium quantities. In GTC, we use extra grid points between every two turbulence grid points for generating the equilibrium mesh, on which equilibrium magnetic fields are calculated and used to push particles. Also note that the QSTK has 6 field periods ($N_{\rm fp}=6$), while the W7-X stellarator has 5 field periods ($N_{\rm fp}=5$) i.e. all equilibrium quantities have a periodicity of $2\pi/N_{\rm fp}$ in the toroidal direction. Therefore, we have constructed the spline on the equilibrium mesh for a field period of $\zeta=[0,2\pi/N_{\rm fp}]$ with the toroidal periodicity explicitly enforced at $\zeta=0$ and $2\pi/N_{\rm fp}$. We exploit the $2\pi/N_{\rm fp}$ periodicity, to simulate one period of each configuration, instead of the full torus.

In the present work, we assume that the electrons follow a Boltzmann distribution. The collisionless gyrokinetic Vlasov equation, which describes the thermal ions in an inhomogeneous magnetic field, is given by [25, 26, 48]

$$\frac{\mathrm{d}}{\mathrm{d}t} f(\mathbf{X}, \mu, \nu_{||}, t) = \left[\frac{\partial}{\partial t} + \dot{\mathbf{X}} \cdot \nabla + \dot{\nu}_{||} \frac{\partial}{\partial \nu_{||}} \right] f = 0;$$

$$\dot{\mathbf{X}} = \nu_{||} \mathbf{b} + \mathbf{v_d} + \mathbf{v_E} \tag{1}$$

where,
$$\begin{split} \dot{v}_{||} &= -\frac{1}{m}\frac{\pmb{B}^*}{B} \cdot (\mu \nabla B + Z_{\rm i} \nabla \phi) \\ & \mathbf{v_d} \,=\, \frac{v_{||}^2}{\Omega} \, (\nabla \times \pmb{b}) + \frac{\mu}{m\Omega} \, (\pmb{b} \times \nabla B) \\ & \mathbf{v_E} \,=\, \frac{c}{B} \, (\pmb{b} \times \nabla \phi) \end{split}$$

where $f(\mathbf{X}, \mu, \nu_{||}, t)$ is the particle distribution function, with \mathbf{X} is the gyrocenter position, μ is the magnetic moment, $\nu_{||}$ is the parallel velocity, $Z_{\mathbf{i}}$ is the ion charge, m is ion mass, and ϕ is the electrostatic perturbed potential. \mathbf{B} is the equilibrium magnetic field at the particle position, $\mathbf{B}^* = \mathbf{B} + \frac{B\nu_{||}}{\Omega} \nabla \times \mathbf{b}$, and $\mathbf{b} = \frac{\mathbf{B}}{B}$. In the present work, we retain the ZF generated by the ITG turbulence, while neglecting the equilibrium radial electric field.

To reduce the particle noise in the simulation, GTC uses the δf method [49]. In this scheme, we decompose the distribution function into an unperturbed equilibrium part and a perturbed part as $f = f_0 + \delta f$. Further, the propagator in equation (1) can be separated into an equilibrium part L_0 and a perturbed part, δL so that the equation (1) can be written as $(L_0 + \delta L)(f_0 + \delta f) = 0$, where

$$L_{0} = \frac{\partial}{\partial t} + (v_{||}\mathbf{b} + \mathbf{v_{d}}) \cdot \nabla - \frac{1}{m} \frac{\mathbf{B}^{*}}{B} \cdot (\mu \nabla B) \frac{\partial}{\partial v_{||}}$$
$$\delta L = \mathbf{v_{E}} \cdot \nabla - \frac{1}{m} \frac{\mathbf{B}^{*}}{B} \cdot Z_{i} \nabla \phi \frac{\partial}{\partial v_{||}}.$$

The equilibrium distribution function f_0 is determined by the condition $L_0 f_0 = 0$. The solution of this equation is approximated to be the local Maxwellian

$$f_0 = \frac{n_{\rm i}}{\left(2\pi T_{\rm i}/m\right)^{3/2}} \exp\left(-\frac{2\mu B + mv_{||}^2}{2T_{\rm i}}\right)$$

where n_i and T_i are the equilibrium ion density and temperature, respectively. Next, we define the particle weight $w = \delta f/f_0$, and the evolution of this dynamical variable corresponding to thermal ions is given by

$$\frac{\mathrm{d}w}{\mathrm{d}t} = (1 - w) \left[-\mathbf{v}_{\mathbf{E}} \cdot \frac{\nabla f_0}{f_0} + \frac{Z_i}{mf_0} \frac{\mathbf{B}^*}{\mathbf{B}} \cdot \nabla \phi \frac{\partial f_0}{\partial v_{||}} \right]. \tag{2}$$

We note from equation (2) that we have neglected the neoclassical effect, since the term $\mathbf{v_d} \cdot \nabla f_0$ does not appear in the above equation. The electrostatic potential ϕ is obtained from the following gyrokinetic Poisson equation [37, 38, 50],

$$\phi - \tilde{\phi} = \frac{T_{\rm i}}{n_{\rm i} Z_{\rm i}^2} (Z_{\rm i} \bar{n}_{\rm i} - e n_{\rm e}), \qquad (3)$$

where $\bar{\phi}$ is the second gyro averaged potential, \bar{n}_i and n_e are the ion and electron guiding center density, respectively. In GTC, we can decompose the electrostatic potential ϕ and ion density perturbation \bar{n}_i into zonal and non-zonal components as

$$\phi = \langle \phi \rangle + \delta \phi,$$

$$\bar{n}_{i} = \langle \bar{n}_{i} \rangle + \delta \bar{n}_{i},$$

with $\langle \delta \phi \rangle = 0$, $\langle \delta \bar{n}_i \rangle = 0$, $\langle \delta n_e \rangle = 0$ and the $\langle \cdots \rangle$ represent flux-surface averaging. The non-zonal part of gyrokinetic Poisson equation thus becomes

$$\delta\phi - \delta\tilde{\phi} = \frac{T_{\rm i}}{n_{\rm i}Z_{\rm i}^2} \left(Z_{\rm i} \, \delta\bar{n}_{\rm i} - e \, \delta n_{\rm e} \right) \, ; \tag{4}$$

$$\delta \tilde{\phi} = \frac{1}{2\pi} \int d^3 \mathbf{v} \int d^3 \mathbf{X} f_0(\mathbf{X}) \, \delta \bar{\phi}(\mathbf{X}) \, \delta(\mathbf{X} + \boldsymbol{\rho} - \mathbf{x}) \quad (5)$$

where $\delta n_{\rm e} = n_{0\rm e}\delta\phi/T_{\rm e}$, $T_{\rm e}$ is the electron temperature. **x** and **X** are the particle position and the particle guiding center position

coordinates, respectively, and ρ is the gyro-radius vector. $\delta \bar{\phi}$ is the first gyro-averaged perturbed potential given by

$$\delta \bar{\phi}(\mathbf{X}) = \int d^3 \mathbf{x} \int \frac{d\alpha}{2\pi} \, \delta \phi(\mathbf{x}) \, \delta(\mathbf{x} - \mathbf{X} - \boldsymbol{\rho}),$$

where α denotes the gyro-phase. Similarly, the ion perturbed density at the location of the guiding center is given by

$$\delta \bar{n}_{i}(\mathbf{x}) = \int d^{3}\mathbf{X} \int \frac{d\alpha}{2\pi} \, \delta f(\mathbf{X}) \, \, \delta\left(\mathbf{x} - \mathbf{X} - \boldsymbol{\rho}\right).$$

A finite difference method is used to obtain the non-zonal electrostatic potential, while the flux-surface average gyrokinetic equation for the zonal component of electrostatic potential is computed using traditional integration in GTC.

3. Linear simulation of ITG in stellarators

3.1. ITG instability in W7-X

We apply the same plasma profiles for both QSTK and W7-X to simulate the linear and nonlinear physics of ITG turbulence in the two optimized stellarators and the effect of ZF. In figures 2 and 3 we show the temperature profile and safety factor, respectively, for W7-X and QSTK. The ion density $n_{\rm i}$, electron density $n_{\rm e}$, and electron temperature $T_{\rm e}$ are assumed to be constant along radius, i.e. $\eta_{\rm i}=\infty$. The definition of radial coordinate is $r=a\sqrt{\psi/\psi_{\rm w}}$, with a the minor radius corresponding to $\psi_{\rm w}$. The temperature gradient length scale, measured relative to the minor radius a, is defined as

$$\left(\frac{a}{L_{T_m}}\right) = -2\frac{\partial \ln T_m}{\partial \tilde{\psi}} \sqrt{\tilde{\psi}}, \text{ where } \frac{1}{L_{T_m}} = -\frac{\partial \ln T_m}{\partial r}$$
 (6)

Here, $\psi = \psi/\psi_w$, with $m = \{i,e\}$ and ψ_w represents the flux at the last close flux surface. The boundaries of the radial simulation domain are $\psi_{\text{inner}} = 0.05 \psi_{\text{w}}$ and $\psi_{\text{outer}} = 0.7 \psi_{\text{w}}$. The maximum value of the ITG length scale measured relative to minor radius is 1.21 as shown in figure 2. Other parameters used in the simulation are major radius $R_0 = 5.58$ m, magnetic field on axis $B_0 = 2.79$ T and electron temperature $T_e = 6.50$ keV. After the convergence test, we use 9 parallel grid points, 121 radial grid points, 4400 poloidal grid points, 200 ions per cell, and $\Delta t = 0.01 R_0 / C_s$ where $C_s / R_0 = 14.11 \times 10^4 \text{s}^{-1}$ and $C_{\rm s} = \sqrt{T_{\rm e}/m_{\rm i}}$ is the ion acoustic speed. Figure 4(left) represents the electrostatic potential of ITG mode on $\zeta = 0$ poloidal plane during the linear phase of the nonlinear simulation at $t = 25.0R_0/C_s$. The mode is localized at the outer mid-plane, where the curvature is bad in the toroidal angle with a beanshape cross section, and it peaks around $\psi \sim 0.51 \psi_{\rm w}$. The mode amplitude peaks at the flux value where the poloidal harmonic number is m = 82, and the corresponding toroidal harmonic number is n = 71 with a frequency of $w_r = 1.54C_s/R_0$. The mode propagates in the ion diamagnetic direction having a growth rate of $\gamma = 0.51C_s/R_0$, and normalized perpendicular wave number $k_{\perp}\rho_{\rm i}=0.55$.

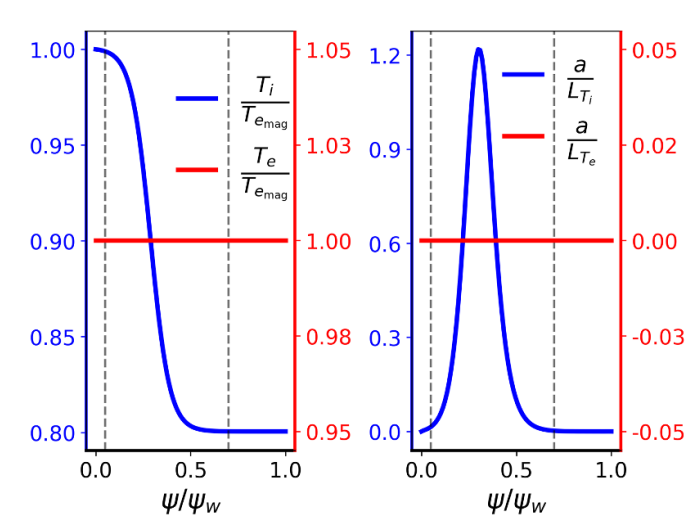


Figure 2. (Left) radial profiles of equilibrium ion (blue) and electron (red) temperatures. Both quantities are normalized by $T_{e_{\text{mag}}}$, the electron temperature on-axis. (Right) we plot the quantity a/L_{T_m} { $m = \{\text{ions, electrons}\}$ } as defined in equation (6). The dashed vertical lines indicate the simulation domain.

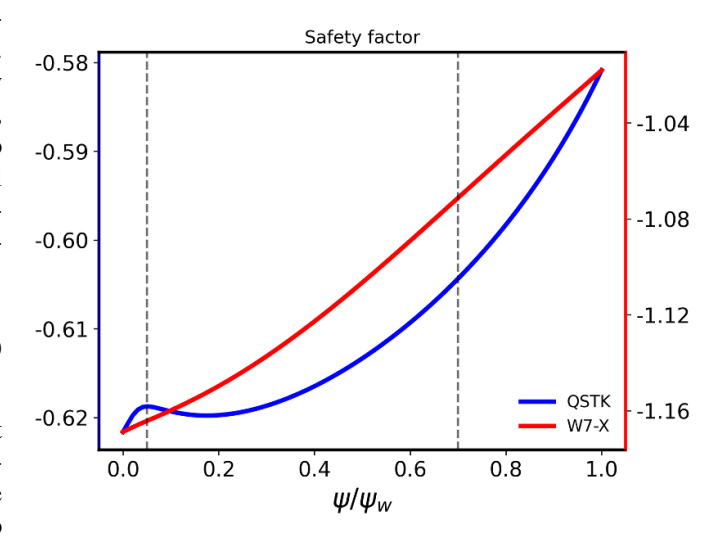


Figure 3. Safety factor (q) for both W7-X (red) and QSTK (blue) are shown in continuous curve and the dashed lines indicate the simulation domain.

3.2. ITG instability in QSTK

The linear ITG simulations for QSTK employ identical spatial resolutions and plasma profiles as those utilized in above analysis for W7-X. The simulation domain is restricted to $\psi_{\text{outer}} = 0.7\psi_{\text{w}}$ due to numerical issues in the QSTK EFIT data. The plasma profile parameters are carefully chosen to ensure the mode is localized within the computational domain, preventing boundary artifacts. The simulation time step used for the linear simulation is $\Delta t = 0.02R_0/C_s$ with $C_s/R_0 = 9.37 \times 10^4$ sec⁻¹. Furthermore, the major radius for the QSTK is $R_0 = 8.40$ m, and the magnetic field on axis value is $B_0 = 1.01$ T. In figure 4(right) we show the mode structure of the electrostatic potential of ITG on the $\zeta = 0$ poloidal plane for QSTK

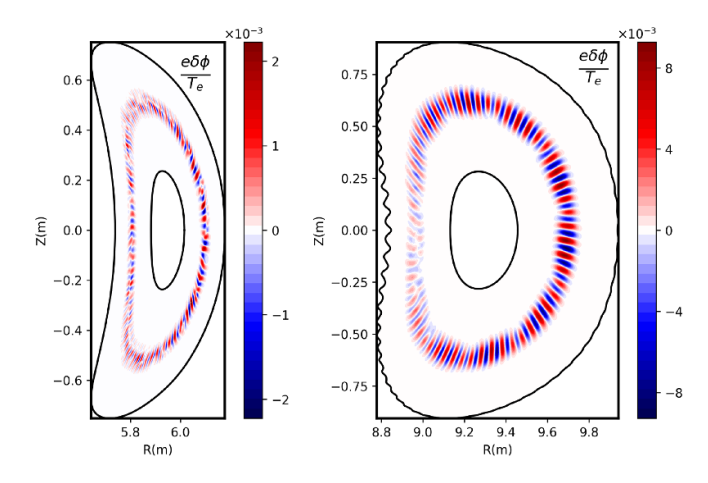


Figure 4. The normalized electrostatic perturbed potential, $e\delta\phi/T_e$, on the $\zeta=0$ poloidal plane in the linear phase, at $t=25.0R_0/C_s$ for W7-X (left) and at $t=37.5R_0/C_s$ for QSTK (right) with the ITG $a/L_{T_i}=1.21$. The black curves represent the inner and outer simulation boundaries. We choose the simulation domain upto $\psi_{\text{outer}}=0.7\psi_{\text{w}}$ since there is a numerical issue with the EFIT data in QSTK. Also, we choose the plasma profile in a manner so that the mode does not spreads to the boundary of domain.

during the growing phase of the nonlinear simulation at t = $37.5R_0/C_s$. The poloidal mode number and the toroidal mode numbers at the location where the eigenmode peaks ($\psi \sim$ $0.52\psi_{\rm w}$) are m=59 and n=63, respectively, with a frequency $w_{\rm r} = 2.64 C_{\rm s}/R_0$ propagating in the ion diamagnetic direction with growth rate $\gamma = 0.35 \ C_s/R_0$ and normalized wave number $k_{\perp}\rho_{\rm i}$ =0.75. While the normalized temperature gradient a/L_{T_i} is chosen to be the same in both QSTK and W7-X cases, the absolute ITG length scale L_{T_i} differs due to differences in the local geometry and equilibrium parameters. In both QSTK and W7-X, the linear mode structures of ITG resemble the typical ballooning structure, localized on the outer midplane, and the widths of the linear modes (full width at half maximum) for both stellarators have almost similar values of 0.06 in units of r/a. At both sides of the radial simulation domain, fixed boundary conditions are applied for all fluctuating quantities, and all the out-of-boundary particles are brought back into the simulation domain through energy-conserving boundary conditions and by setting particle weight to be zero.

4. Nonlinear ITG simulations

In this section, we focus on the turbulence features for QSTK and W7-X using the same plasma profiles. Specifically, we study the effect of ZFs on the collisionless ITG saturation mechanism in both W7-X and QSTK. The spatial resolutions and the marker particle numbers for these nonlinear simulations are the same as the linear cases; however, the time step for these simulations is $\Delta t = 0.01R_0/C_s$. Figure 5 represents the contour plots of the electrostatic potential in the nonlinear phase of ITG micro-turbulence in the absence (via numerical suppression) and presence of ZFs for the QSTK and W7-X stellarators. When ZFs are artificially removed in the nonlinear phase, the linear mode structure spreads radially from

the linear eigenmode due to nonlinear toroidal mode coupling figures 5(a) and (c). Once we include ZFs in the simulation, the zonal shear breaks these eddies into fine structures figures 5(b) and (d) similar to turbulent self-regulation by ZFs in the tokamak [35]. To demonstrate the effect of ZFs on the electrostatic potential, we have calculated the root-meansquare value of $\delta \phi$ in the absence and presence of ZFs as the flux surface averaged radial electric field generated by turbulence at the nonlinear stage at $t = 55R_0/C_s$, and for QSTK at $t = 65R_0/C_s$, see figure (6). The difference in turbulence potential, shown by the red and blue lines, highlights the suppression of ITG turbulence by ZFs in both configurations. In W7-X, the suppression is \sim 2.1 times, while in QSTK, it is \sim 5.9 times, including ZFs, compared to the case without ZFs. This demonstrates the significant role of ZFs in reducing ITG-driven turbulent transport [25] in these two optimized stellarators.

To further evaluate the ZF effect, we have analyzed the poloidal spectrum of the time-averaged electrostatic potential during the nonlinear phase. Figure 7 shows the time-averaged poloidal wave number spectrum for QSTK (left) and W7-X (right) in the presence and absence of ZFs. For QSTK, we consider the time average from $65.05R_0/C_s$ to $72.5R_0/C_s$ and for W7-X, from 47.5 R_0/C_s to 52.5 R_0/C_s . The wave number spectra are broad due to the nonlinear mode coupling $k_{\theta} \in [0, 0.15] \text{ mm}^{-1} \text{ and } k_{\theta} \in [0, 0.4] \text{ mm}^{-1} \text{ for QSTK and}$ W7-X, respectively, in the absence of ZFs. Interestingly, in figure 7, it is shown that the poloidal wave numbers move to a rather low value for QSTK, whereas high poloidal wave numbers still dominate for W7-X. We conjecture that this is a result of the effects of CG optimization, which, by increasing the gradient of the binormal coordinate along magnetic field lines (see figure 8), stabilizes ITG modes with large poloidal wavenumbers relative to those with lower wavenumbers. The resulting low wavenumber modes are driven more weakly by

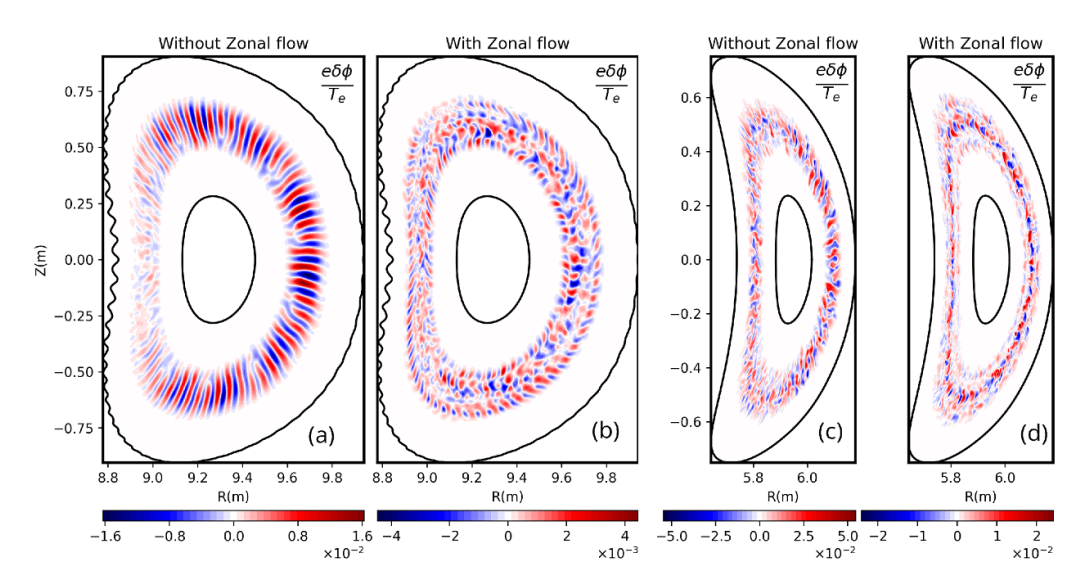


Figure 5. Contour plots of the electrostatic perturbed potential in the nonlinear phase for both machines with ion temperature gradient $a/L_{T_i} = 1.21$. (a) QSTK without ZFs, (b) QSTK with ZFs at $t = 55.0R_0/C_s$, (c) W7-X without ZFs, (d) W7-X with ZFs at $t = 45.0R_0/C_s$. The black curves indicate the inner and outer simulation boundaries.

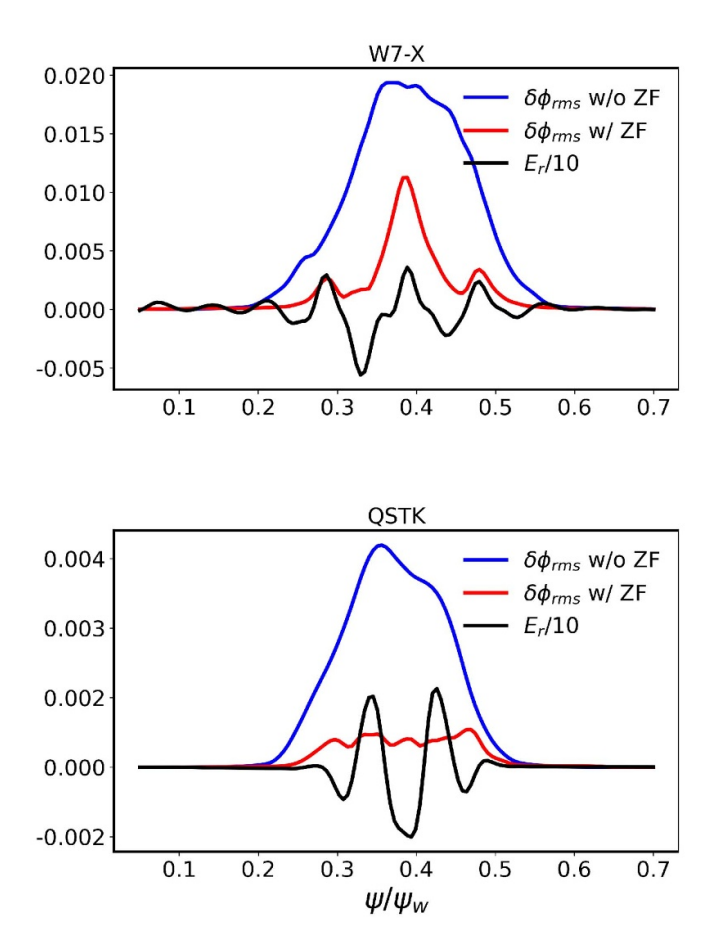


Figure 6. The flux surface variation of root-mean-squared electrostatic perturbed potential ($\delta\phi_{\rm rms}$) with (blue line) and without (red line) ZF and the radial electric field ($E_{\rm r}$) (black line) from the turbulence at the saturation stage of ITG turbulence at time $t=55R_0/C_{\rm s}$ for W7-X (top) and $t=65R_0/C_{\rm s}$ QSTK (bottom). The electrostatic potential is normalized with $T_{\rm e}/e$, and the radial electric field resulting from the turbulence is normalized with $\sqrt{T_{\rm e}/e}$. The ion temperature gradient, in this case, is $a/L_{T_{\rm i}}=1.21$.

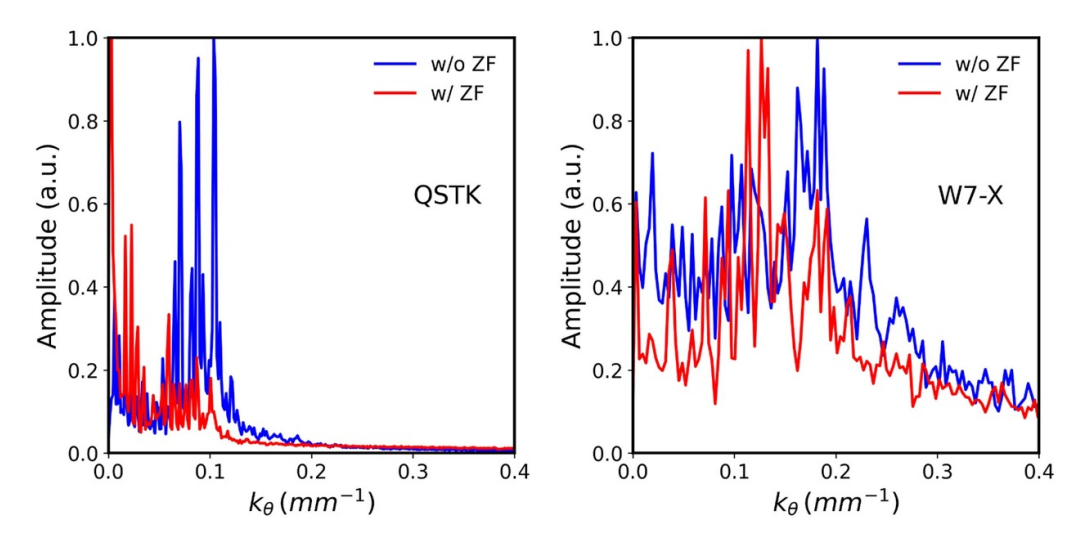


Figure 7. The poloidal wave number spectrum in QSTK (Left) and W7-X (Right) for the ion temperature gradient $a/L_{T_i} = 1.21$. The poloidal wave number decreases for both configurations in the presence of ZFs. For QSTK, the poloidal spectrum is plotted by taking the average over the saturation phase $t = [65.0, 72.5]R_0/C_s$ with and without ZFs. For W7-X, the same quantity is plotted by averaging over $t = [32.5, 40]R_0/C_s$ with and without ZFs.

toroidal curvature (through the drift factor \mathbf{v}_d in the gyrokinetic equation) and are thus expected to have smaller relative growth rates.

Finally, to quantify the ZF effect on micro-turbulence, we computed the transport coefficients in these two configurations in the presence and absence of ZFs. Figure 9(a) shows the time trace of ion heat conductivity, which is calculated in GTC as [37]

$$\chi_{i} = \frac{1}{\langle |\nabla \psi|^{2} \rangle n_{i} \frac{\partial T_{i}}{\partial \psi}} \left\langle \int d^{3}v \delta f \left(\frac{1}{2} m_{i} v^{2} - \frac{3}{2} T_{i} \right) \mathbf{v}_{E} \cdot \nabla \psi \right\rangle.$$
(7)

To calculate the above quantity, we first evaluate the term in numerator and the terms $\langle |\nabla \psi|^2 \rangle n_i$ in denominator. We then divide the whole quantity by the maximum value of $\partial T_i/\partial \psi$ (as shown in figure 2) to get the value of χ_i . We calculate the reduction due to ZFs by taking the mean value of the χ_i in the saturated regime as shown in figure 9(a). The results for this reduction is presented in table 1. We also performed a scan in ITGs $(a/L_{T_i} = [1.21, 2.42, 3.63])$, retaining ZFs, and calculated the normalized ion heat diffusivity in the figure 9(b). QSTK has lower ion heat diffusivity over the entire

range of gradients, even above the apparent ITG threshold near $a/L_{T_i} = 1.2$. The more modest (though still significant) suppression factors at higher gradients are expected once the CGs of both configurations are exceeded, as appears to be the case in light of the a/L_T scan shown in figure 9(b), since both configurations produce finite heat fluxes at these gradients. In figures 9(c) and (e), we present the time evolution of the radial profile of χ_i for QSTK and W7-X, respectively. Similarly, in figures 9(d) and (f), we plot the corresponding shearing rate defined as $\omega_{\rm E} = (\partial^2 \langle \phi \rangle / \partial \psi^2) (\Delta r / \Delta \theta) R B_{\theta} / q$ [51] where, Δr and $r\Delta\theta$ are the radial and poloidal correlation lengths, respectively, and B_{θ} is the poloidal magnetic field. We assume that the radial and poloidal correlation lengths are equal for the purpose of evaluating ω_E . We observe that W7-X exhibits a higher shearing rate than QSTK. The ZF generated during nonlinear ITG saturation is rapidly damped by collisionless magnetic pumping effects [52], resulting in a lower residual level. Linear GTC simulations indicate higher residual levels for QSTK (0.48) compared to W7-X (0.27). A key feature of figures 9(c)–(f) is that the nonlinear frequency of ZF in W7-X is higher than in QSTK. Additionally, the radial structure of QSTK is more coherent and stable than that of W7-X, suggesting a stronger nonlinear instability of ZFs in W7-X.

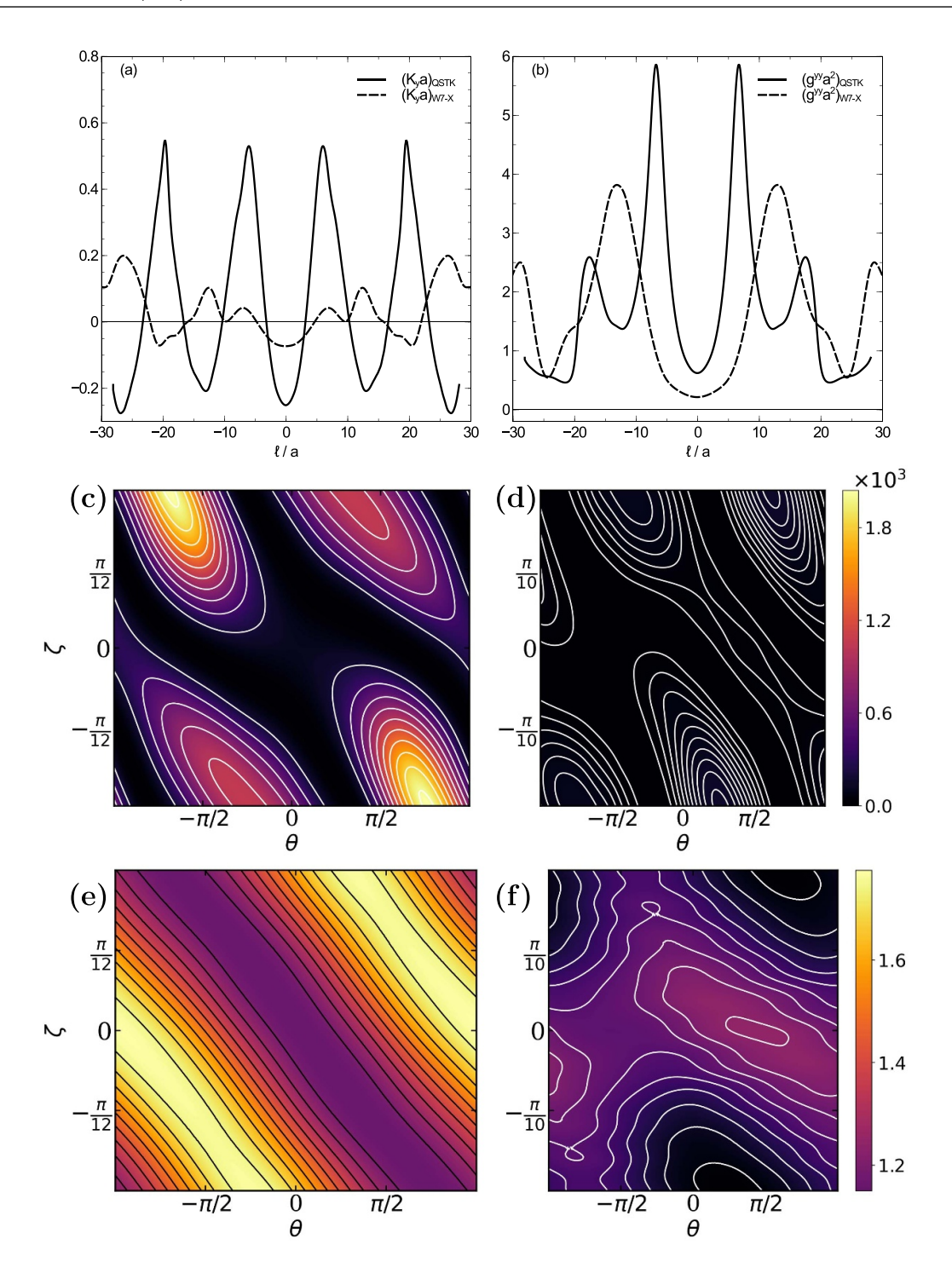


Figure 8. Geometric quantities entering the gyrokinetic equation, plotted along the standard flux tube on the outboard midplane at $\zeta=0$, illustrating the difference in drift curvature and squared gradient of the binormal coordinate ∇y at the radius $\psi/\psi_{\rm edge}=0.25$, for both QSTK and W7-X. The y coordinate corresponds to the field line label α , $\mathbf{B}=\nabla\psi\times\nabla\alpha$, such that $y=\sqrt{\psi_0/\psi_w}\,(q(\theta-\theta_0)-\zeta)$, with ψ_0 the chosen flux surface, q_0 the safety factor at that surface, and θ_0 the ballooning angle. The horizontal axes of both plots are in units of arc length normalized to the respective minor radius a of each configuration, while the vertical axes are dimensionless but also normalized to the minor radius of each respective configuration. One toroidal turn is chosen for the extent along the field line in both cases. (a) The drift curvature $K_y=(1/B^2)\mathbf{B}\times\nabla B\cdot\nabla y$ showing a narrower connection length between 'good' (positive) and 'bad' (negative) curvature for QSTK compared to W7-X. (b) Plotting $g^{yy}=|\nabla y|^2$ shows that that $|\nabla y|^2$ is noticeably larger for QSTK at the central unstable bad curvature well near $\ell=0$, suggesting enhanced finite Larmor radius stabilization at larger poloidal wavenumbers. We also plot the metric quantities using the GTC code. $g_{\theta\theta}$ for (c) QSTK and (d) for W7-X. $g_{\zeta\zeta}$ for (e) QSTK and (f) for W7-X.

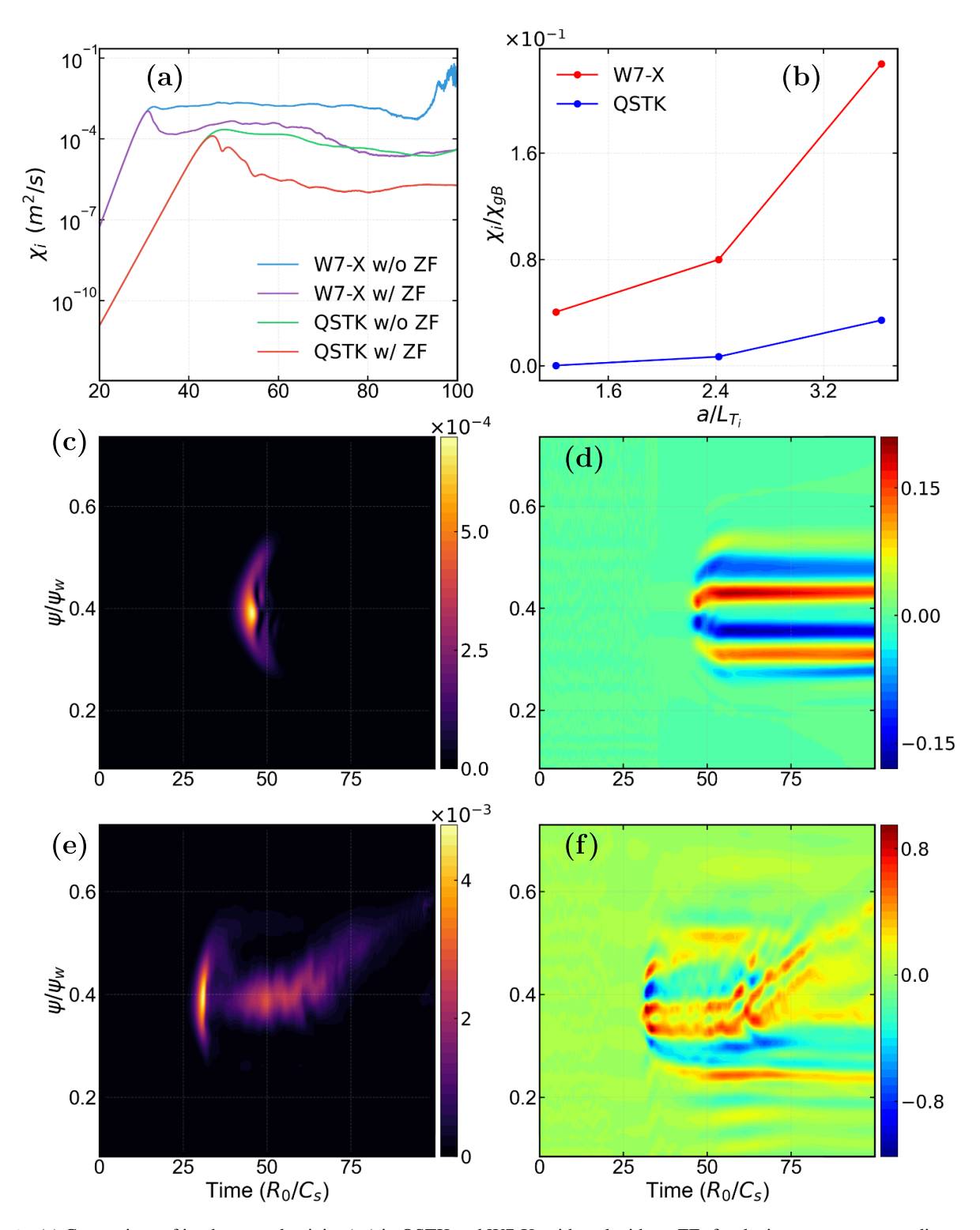


Figure 9. (a) Comparison of ion heat conductivity (χ_i) in QSTK and W7-X, with and without ZFs for the ion temperature gradient $a/L_{T_i}=1.21$. We find that there is a numerical instability for the case of without ZF in the case of W7-X at late times. (b) In the presence of ZFs, the normalized ion heat diffusivity in gyro-Bohm units is plotted as a function of the ion temperature gradient. We see that the normalized ion heat diffusivity is lower in QSTK compared to the W7-X over the entire range of ion temperature gradient. The time evolution of the radial profile of χ_i for QSTK and W7-X is shown in (c) and (e), while the corresponding shearing rates are presented in (d) and (f), respectively, for $a/L_{T_i}=1.21$.

Table 1. Comparison of the effect of ZF for the two stellarators. We compare the ion heat conductivity (χ_i) in the nonlinear regime for the two cases listed below. The reduction $(=\chi_{i_{woZF}}/\chi_{i_{wzI}})$ is calculated by taking the ratio of the mean of χ_i in the nonlinear regime shown in figure 9(a). We also compare the effect of temperature gradient on the reduction of χ_i in the presence of ZFs in the two machines.

Case	$a/L_{T_{\mathrm{i}}}$	Reduction in χ_i
W7-X (w/o ZF) vs QSTK (w/o ZF)	1.21	~34.12
W7-X (w/ZF) vs QSTK(w/ZF)	1.21	$\sim \! 27.25$
W7-X (w/ZF) vs QSTK(w/ZF)	2.42	~ 8.6
W7-X (w/ZF) vs QSTK(w/ZF)	3.63	\sim 4.9

5. Conclusion and discussion

In this work we have carried out the study of ITG-driven turbulence in the optimized stellarators W7-X and QSTK. The latter design resulted from a recent optimization study that targeted the CG of the ITG mode [10]. We found a sensitivity of the turbulence saturation level on the ZFs. The ion heat flux, differed by a large factor (\sim 34) between the two stellarators at the lowest gradient, where QSTK is close to the ITG marginality. Such a large relative factor at this gradient suggests a threshold behavior in line with the targeting of a high linear CG for ITG modes in QSTK. At higher temperature gradients, apparently above this threshold, QSTK continues to enjoy lower nonlinear heat fluxes in comparison to W7-X, perhaps in part because of reduced linear growth rates for ITG modes. We thus expect CG optimization to continue to be useful in guiding stellarator design for reduced ion transport, whether as a result of improved thresholds at low gradients, lower growth rates at high gradients, or through some interplay of the two effects. ZF generation is more pronounced when ITG turbulence is near marginal stability, i.e. when the linear growth rate is low. In such conditions, ZFs can persist longer and effectively suppress turbulent transport, as illustrated in figure 9. This study provides valuable insights into how 3D geometries, such as QSTK and W7-X stellarators offer a crucial tool for designing and optimising new stellarators. However, the ultimate determinant of a stellarator's feasibility as a fusion reactor will be the level of turbulent transport, with the ability to self-regulate playing a pivotal role. The present focus of this paper is to study the ZF physics with adiabatic electrons. However, the kinetic electrons will play a significant role in evaluating more accurate heat flux as described in detail in [25, 53, 54], which will be carried out in future work.

Data availability statement

Given the complex nature of the data and the associated privacy and confidentiality issues, we can share it only upon request. The data that support the findings of this study are available upon reasonable request from the authors.

Acknowledgments

This work is supported by Board of Research in Nuclear Sciences (BRNS Sanctioned No. and 57/14/04/2022-BRNS), Science and Engineering Research Board EMEQ program (SERB sanctioned No. EEQ/2022/000144), National Supercomputing Mission (NSM), US Department of Energy under Award Nos. DE-SC0024548 and DE-FG02-07ER54916. We acknowledge National Supercomputing Mission (NSM) for providing computing resources of 'PARAM PRAVEGA' at S.E.R.C. Building, IISc Main Campus Bangalore, which is implemented by C-DAC and supported by the Ministry of Electronics and Information Technology (MeitY) and Department of Science and Technology (DST), Government of India, ANTYA cluster at Institute of Plasma Research, Gujarat, and by US DOE SciDAC and INCITE. A T thanks the University Grants Commission (UGC) for supporting him as a Senior Research Fellow (SRF).

ORCID iDs

Abhishek Tiwari © 0009-0005-7836-751X

Joydeep Das © 0009-0006-3179-0174

Jaya Kumar Alageshan © 0000-0003-0351-1992

Gareth Roberg-Clark © 0000-0001-5280-2644

Gabriel Plunk © 0000-0002-4012-4038

Pavlos Xanthopoulos © 0000-0003-3545-4822

Sarveshwar Sharma © 0000-0002-0642-0247

Zhihong Lin © 0000-0003-2007-8983

Animesh Kuley © 0000-0003-2325-6597

References

- [1] Velasco J L, Calvo I, Escoto F J, Sánchez E, Thienpondt H and Parra F I 2024 Piecewise omnigenous stellarators *Phys. Rev. Lett.* 133 185101
- [2] Lion J et al 2025 Stellaris: a high-field quasi-isodynamic stellarator for a prototypical fusion power plant Fusion Eng. Des. 214 114868
- [3] Nicolau J H, Choi G, Fu J, Liu P, Wei X and Lin Z 2021 Global gyrokinetic simulation with kinetic electron for collisionless damping of zonal flow in stellarators *Nucl. Fusion* 61 126041
- [4] Mishchenko A, Helander P and Könies A 2008 Collisionless dynamics of zonal flows in stellarator geometry *Phys. Plasmas* 15 072309
- [5] Beidler C D et al 2021 Demonstration of reduced neoclassical energy transport in Wendelstein 7-X Nature 596 221–6
- [6] Dinklage A et al 2018 Magnetic configuration effects on the Wendelstein 7-X stellarator Nat. Phys. 14 855–60
- [7] Carralero D et al (the Wendelstein 7-X team) 2021 An experimental characterization of core turbulence regimes in wendelstein 7-X Nucl. Fusion 61 096015
- [8] Beurskens M N A et al (the W7-X Team) 2021 Ion temperature clamping in wendelstein 7-X electron cyclotron heated plasmas Nucl. Fusion 61 116072
- [9] Edlund E M, Porkolab M, Huang Z, Grulke O, Böttger L-G, von Sehren C and von Stechow A 2018 Overview of the Wendelstein 7-X phase contrast imaging diagnostic *Rev.* Sci. Instrum. 89 10E105

- [10] Roberg-Clark G T, Plunk G G, Xanthopoulos P, Nührenberg C, Henneberg S A and Smith H M 2023 Critical gradient turbulence optimization toward a compact stellarator reactor concept *Phys. Rev. Res.* 5 L032030
- [11] Podavini L, Zocco A, García-Rega na J M, Barnes M, Parra F I, Mishchenko A and Helander P 2024 Ion temperature and density gradient driven instabilities and turbulence in wendelstein 7-X close to the stability threshold J. Plasma Phys. 90 905900414
- [12] Kuley A and Tripathi. V K 2009 Stabilization of ion temperature gradient driven modes by lower hybrid wave in a tokamak *Phys. Plasmas* 16 032504
- [13] Kuley A, Liu C S and Tripathi V K 2010 Lower hybrid destabilization of trapped electron modes in tokamak and its consequences for anomalous diffusion *Phys. Plasmas* 17 072506
- [14] Kleiber R et al 2024 Euterpe: a global gyrokinetic code for stellarator geometry Comput. Phys. Commun. 295 109013
- [15] Riemann J et al (the Wendelstein 7-X Team 2025 Excitation of alfvénic modes via electromagnetic turbulence in wendelstein 7-X Phys. Rev. Lett. 134 025103
- [16] Riemann J, Kleiber R and Borchardt M 2016 Effects of radial electric fields on linear itg instabilities in W7-X and LHD Plasma Phys. Control. Fusion 58 074001
- [17] Thienpondt H, García-Rega na J M, Calvo I, Acton G and Barnes M 2024 Influence of the density gradient on turbulent heat transport at ion-scales: an inter-machine study with the gyrokinetic code stella *Nucl. Fusion* 65 016062
- [18] Nakata M, Nunami M, Sugama H and Watanabe T-H 2017 Isotope effects on trapped-electron-mode driven turbulence and zonal flows in helical and tokamak plasmas *Phys. Rev.* Lett. 118 165002
- [19] Mynick H E, Pomphrey N and Xanthopoulos P 2011 Reducing turbulent transport in toroidal configurations via shaping Phys. Plasmas 18 056101
- [20] Navarro A B, Di Siena A, Velasco J L, Wilms F, Merlo G, Windisch T, LoDestro L L, Parker J B and Jenko F 2023 First-principles based plasma profile predictions for optimized stellarators *Nucl. Fusion* 63 054003
- [21] Navarro A B, Roberg-Clark G T, Plunk G G, Fernando D, Di Siena A, Wilms F and Jenko F 2024 Assessing core ion thermal confinement in critical-gradient-optimized stellarators *Phys. Plasmas* 31 062508
- [22] Matsuoka S, Idomura Y and Satake S 2018 Neoclassical transport benchmark of global full-f gyrokinetic simulation in stellarator configurations *Phys. Plasmas* 25 022510
- [23] Cole M D J, Moritaka T, Hager R, Dominski J, Ku S and Chang C S 2020 Nonlinear global gyrokinetic delta-f turbulence simulations in a quasi-axisymmetric stellarator *Phys. Plasmas* 27 044501
- [24] Navarro A B, Merlo G, Plunk G G, Xanthopoulos P, von Stechow A, Di Siena A, Maurer M, Hindenlang F, Wilms F and Jenko F 2020 Global gyrokinetic simulations of ITG turbulence in the magnetic configuration space of the wendelstein 7-X stellarator *Plasma Phys. Control. Fusion* 62 105005
- [25] Singh T, Nicolau J H, Lin Z, Sharma S, Sen A and Kuley A 2022 Global gyrokinetic simulations of electrostatic microturbulent transport using kinetic electrons in LHD stellarator *Nucl. Fusion* 62 126006
- [26] Singh T, Nicolau J H, Nespoli F, Motojima G, Lin Z, Sen A, Sharma S and Kuley A 2024 Global gyrokinetic simulations of electrostatic microturbulent transport in lhd stellarator with boron impurity *Nucl. Fusion* 64 016007
- [27] Coelho A J, Loizu J, Ricci P and Tecchiolli Z 2024 Global fluid simulation of plasma turbulence in stellarators with the GBS code *Nucl. Fusion* 64 076057

- [28] Shanahan B, Dudson B and Hill P 2018 Fluid simulations of plasma filaments in stellarator geometries with BSTING Plasma Phys. Control. Fusion 61 025007
- [29] Shanahan B, Bold D and Dudson B 2024 Global fluid turbulence simulations in the scrape-off layer of a stellarator island divertor J. Plasma Phys. 90 905900216
- [30] Wang H Y, Holod I, Lin Z, Bao J, Fu J Y, Liu P F, Nicolau J H, Spong D and Xiao Y 2020 Global gyrokinetic particle simulations of microturbulence in W7-X and LHD stellarators *Phys. Plasmas* 27 082305
- [31] Fu J Y, Nicolau J H, Liu P F, Wei X S, Xiao Y and Lin Z 2021 Global gyrokinetic simulation of neoclassical ambipolar electric field and its effects on microturbulence in W7-X stellarator *Phys. Plasmas* **28** 062309
- [32] Qin Y Q, Chen Y C, Sun G Y, Nicolau J and Lin Z 2024 Effects of hydrogen isotope species on ITG microturbulence in LHD *Plasma Phys. Control. Fusion* 66 085004
- [33] Chen H, Wei X, Zhu H and Lin Z 2025 Geometry effects on zonal flow dynamics and turbulent transport in optimized stellarators *Nucl. Fusion* 65 074002
- [34] Carralero D *et al* (the Wendelstein 7-X Team) 2024 First experimental observation of zonal flows in the optimized stellarator wendelstein 7-X (arXiv:2406.12514)
- [35] Lin Z, Hahm T S, Lee W W, Tang W M and White R B 1998 Turbulent transport reduction by zonal flows: massively parallel simulations *Science* 281 1835–7
- [36] Xiao Y and Lin Z 2009 Turbulent transport of trapped-electron modes in collisionless plasmas Phys. Rev. Lett. 103 085004
- [37] Singh T, Sharma D, Macwan T, Sharma S, Ghosh J, Sen A, Lin Z and Kuley A 2023 Gyrokinetic simulations of electrostatic microturbulence in ADITYA-U tokamak *Nucl.* Fusion 63 056008
- [38] Singh T et al 2024 Gyrokinetic simulations of electrostatic microturbulence in ADITYA-U tokamak with argon impurity Nucl. Fusion 64 086038
- [39] Singh T, Rafiq T, Schuster E, Lin Z and Kuley A 2024 Global gyrokinetic simulations of kinetic ballooning mode in NSTX-U plasmas *Bull. Am. Phys. Soc.* (available at: https://physics.iisc.ac.in/~akuley/Papers/Tajinder25.pdf)
- [40] Wang Z, Lin Z, Holod I, Heidbrink W W, Tobias B, Van Zeeland M and Austin M E 2013 Radial localization of toroidicity-induced alfvén eigenmodes *Phys. Rev. Lett.* 111 145003
- [41] Liu P, Wei X, Lin Z, Brochard G, Choi G J, Heidbrink W W, Nicolau J H and McKee G R 2022 Regulation of alfvén eigenmodes by microturbulence in fusion plasmas *Phys.* Rev. Lett. 128 185001
- [42] Zhang W, Lin Z and Chen L 2008 Transport of energetic particles by microturbulence in magnetized plasmas *Phys. Rev. Lett.* 101 095001
- [43] Brochard G et al 2024 Saturation of fishbone instability by self-generated zonal flows in tokamak plasmas Phys. Rev. Lett. 132 075101
- [44] Kuley A, Wang Z X, Lin Z and Wessel F 2013 Verification of particle simulation of radio frequency waves in fusion plasmas *Phys. Plasmas* 20 102515
- [45] Kuley A, Lin Z, Bao J, Wei X S, Xiao Y, Zhang W, Sun G Y and Fisch N J 2015 Verification of nonlinear particle simulation of radio frequency waves in tokamak *Phys. Plasmas* 22 102515
- [46] Bao J, Lin Z, Kuley A and Wang Z X 2016 Electromagnetic particle simulation of the effect of toroidicity on linear mode conversion and absorption of lower hybrid waves *Nucl. Fusion* 56 066007
- [47] Hirshman S P and Whitson J C 1983 Steepest-descent moment method for three-dimensional magnetohydrodynamic equilibria *Phys. Fluids* 26 3553–68

- [48] Brizard A J and Hahm T S 2007 Foundations of nonlinear gyrokinetic theory *Rev. Mod. Phys.* 79 421–68
- [49] Parker S E and Lee W W 1993 A fully nonlinear characteristic method for gyrokinetic simulation *Phys. Fluids B* **5** 77–86, 01
- [50] Lee W W 1987 Gyrokinetic particle simulation model J. Comput. Phys. 72 243–69
- [51] Hahm T S and Burrell K H 1995 Flow shear induced fluctuation suppression in finite aspect ratio shaped tokamak plasma *Phys. Plasmas* 2 1648–51
- [52] Rosenbluth M N and Hinton F L 1998 Poloidal flow driven by ion-temperature-gradient turbulence in tokamaks *Phys. Rev.* Lett. 80 724–7
- [53] García-Rega na J M, Calvo I, Sánchez E, Thienpondt H, Velasco J L and Capitán J A 2024 Reduced electrostatic turbulence in the quasi-isodynamic stellarator configuration CIEMAT-QI4 Nucl. Fusion 65 016036
- [54] Zocco A, Podavini L, Wilms F, Navarro A B and Jenko F 2024 Electron-temperature-gradient-driven ion-scale turbulence in high-performance scenarios in wendelstein 7-X *Phys. Rev. Res.* 6 033099